



POLITECNICO
MILANO 1863

**SCUOLA DI INGEGNERIA INDUSTRIALE
E DELL'INFORMAZIONE**

EXECUTIVE SUMMARY OF THE THESIS

Streamwise traveling waves of wall deformation for turbulent drag reduction

LAUREA MAGISTRALE IN AERONAUTICAL ENGINEERING - INGEGNERIA AERONAUTICA

Author: NIL COUTO OVEJERO

Advisor: PROF. MAURIZIO QUADRIO

Co-advisor:

Academic year: 2023-2024

1. Introduction

The aeronautical industry is facing one of the major challenges in aviation history: the reduction of CO_2 emissions and a transition into a greener industry model. Skin friction drag is a major component of the overall drag of airplanes, cars or other transport vehicles, reason why flow control strategies for drag reduction have been extensively researched for decades. Flow control strategies can be divided in two categories: Passive and Active. Passive flow control techniques are based on geometry modifications that doesn't introduce external energy to the system (e.g riblets), while active techniques introduces energy into the system (e.g traveling waves of blowing or suction or travelling waves of wall deformation). Both approaches have demonstrated to be able to reduce drag under different conditions and drag components (friction drag and pressure drag), even though active flow control shows better drag reduction at the expend of adding complexity in the procedures.

1.1. Objective

The objective of this Thesis is to implement peristaltic moving walls (streamwise traveling waves of wall deformation) with an in-house DNS code

in order to replicate the results obtained by Nakanishi et. al in 2012 [3], and to analyze up to which extent net power saving can be achieved. The in-house DNS code used was first developed by Secchi in 2018 [4], who adapted an already existing Immersed Boundary method flow solver (produced by Paolo Luchini) in order to account also for non-planar moving walls. The code originally used a hard-coded parallelisation scheme. The update of the this scheme in order to exploit the MPI library has been also set as one of the goals of the present Thesis. The in-house code uses an Immersed Boundary method for the wall treatment, allowing to use a non body conformal Cartesian grid constant in time that reduces memory consumption and computational costs.

2. Numerical implementation

2.1. Governing Equations

For the problem considered, the governing equations are the continuity equation and the viscous, unsteady, incompressible momentum equation, which are defined in the following form:

$$\nabla \cdot \mathbf{u} = 0 \quad (1)$$

$$\frac{\partial \mathbf{u}}{\partial t} + (\mathbf{u} \cdot \nabla) \mathbf{u} = -\nabla p + \nu \nabla^2 \mathbf{u} \quad (2)$$

where \mathbf{u} is the velocity vector, p is the pressure P divided by the fluid density ρ and ν is the kinematic viscosity of the fluid. From this point on, quantities in dimensional form are denoted with an asterisk. The Reynolds number is defined as:

$$Re = \frac{U^* h^*}{\nu^*} \quad (3)$$

Where U^* is the reference velocity, h^* the reference length scale and ν^* is the fluid kinematic viscosity. The reference geometry is a plane channel represented by two walls distancing $2\delta^*$. All dimensional variables are made dimensionless by using the mean bulk velocity U_b^* and the half channel height δ^* . As a consequence, the reference bulk Reynolds number is defined as $Re_b = \frac{U_b^* \delta^*}{\nu^*}$

2.2. Immersed Boundary method

As it has been already mentioned, the code exploits the usage of an Immersed Boundary method (IBM). One of the implications of this method is that the boundary conditions can rarely be imposed straight forward because of the the grid doesn't adapt to the solid boundaries but instead it remains constant in time. Therefore, the boundary between solid walls and fluid is usually placed inside of a grid element, which requires a special treatment to impose the boundary conditions. Time advancement is performed using a fully explicit third order Runge-Kutta method with a fractional step technique applied at each sub-step. IBM is characterized by first advancing the governing equations without accounting for the boundary conditions, and a correction to the linear term of the momentum equation is applied afterwards to account for the boundary's location in those elements for which its computational stencil intersect the boundaries. Note that the linear term is responsible of the main contribution in momentum's balance in regions close to the solid boundary.

2.3. Setup of the experiment

The geometry considered in the present project is a channel flow composed of two movable solid walls where no-slip boundary conditions have

to be applied. The code is based on an Immersed Boundary algorithm in order to enforce the boundary conditions. A representation of the geometry is presented in Fig.1.

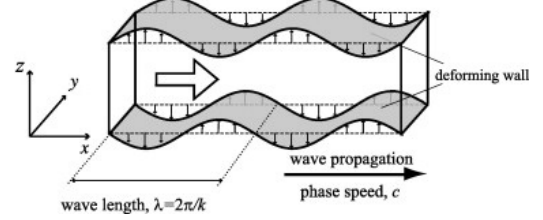


Figure 1: Reference channel geometry with moving walls [3].

The position of the movable walls is defined with the analytic form for the top and bottom solid walls independently, in this case both sinusoidal functions. A similar implementation is followed for the wall velocity boundary condition:

$$\begin{cases} z_b = -\frac{a}{kc} \sin[k(x - ct)] & \text{Lower wall} \\ z_t = 2 + \frac{a}{kc} \sin[k(x - ct)] & \text{Upper wall} \end{cases}$$

$$\begin{cases} u = v = 0, w_b = a \cos[k(x - ct)]; z = z_b \\ u = v = 0, w_t = -a \cos[k(x - ct)]; z = z_t \end{cases}$$

Where a is the wall velocity amplitude, k the wavelength and c is the wave propagation speed of the downstream traveling peristaltic waves. These three parameters will be the input parameters used during the peristalsis tests. The computational domain is defined by $L_x = 4\pi$ and $L_y = 3.5$ in the streamwise and spanwise directions respectively. For the wall normal direction, even if the plane channel height is $2\delta^*$ ($\delta^*=1$), the height of the computational domain has been set to $L_z = 2.2$ in order to have enough space to allocate the walls when peristalsis is applied. The resolution of the grid has been set to $nx = 400$, $ny = 112$ and $nz = 260$. The selection of the domain size and grid resolution was based on previous DNS studies with the same objective [4] [3]. All the simulations have been performed for a $Re_b = 2800$, which corresponds to $Re_\tau \approx 180$ for the turbulent plane channel. After the implementation of the MPI library, a scaling performance study was performed, resulting in a parallel configuration based on $P = 16$ processors divided evenly ($nx = ny = 4$).

3. Results

3.1. Reference case

The reference case corresponds to the uncontrolled turbulent plane channel flow, and likewise to the other simulations included in the Thesis it has been simulated for 1000 external units, with sampling every 10 external units. The validation of the results have been performed by comparing the resulting statistics with those presented by Kim, Moin and Moser [2] (KMM), and collected in Tab.1.

	Validation	KMM [2]
Re_b	2800	≈ 2800
Re_τ	176.4	≈ 180
Re_c	3276	≈ 3300
u_τ	0.063	0.064
δ_ν	0.0055	0.0056
C_f	$8.16 \cdot 10^{-3}$	$8.18 \cdot 10^{-3}$
U_b/u_τ	15.87	15.63
U_c/u_τ	18.57	18.20
U_c/U_b	1.17	1.16

Table 1: Reference case validation

Observing Tab.1 it can be seen how the computed mean flow properties are in great agreement with the reference data, and the small differences in the results may be a consequence of the differences in the mesh resolution and the usage of a spectral method by KMM. The root-mean-square velocity fluctuation components for the reference case u'_{rms} , v'_{rms} , w'_{rms} , normalized by the bulk velocity U_b , can be seen in Fig.6 in black. Both the *rms* fluctuation velocity components and the computed Reynolds shear stress show symmetry with respect to the centerline, which confirms that the solution has reached an statistical steady state, and the shape of the profiles coincide with the theoretical solution.

3.2. Peristalsis Cases

Once the reference case has been established and validated in terms of mean flow properties and flow statistics, the set of controlled simulations as function of the peristalsis inputs presented in Tab.2 were executed and post-processed. The run-time solution of the mean pressure gradients for the peristalsis cases and reference case together with the theoretical laminar solution

are presented in Fig.2.

Case	a	c	k	Case in [3]
Ref. case	0	0	0	-
1	0.3	2	2	8
2	0.3	2	4	9
3	0.4	2	2	11
4	0.2	2	1	4
5	0.1	2	1	1
6	0.2	2	4	6
7	0.1	6	4	14
8	0.1	2	2	2
9	0.2	6	2	15
10	0.2	6	4	16
11	0.4	2	4	12

Table 2: Peristalsis parameters

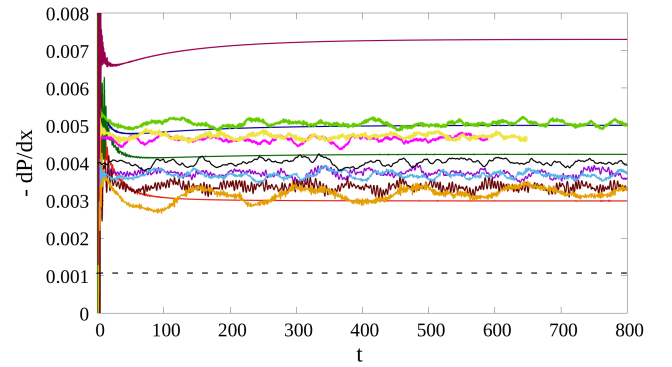


Figure 2: Mean streamwise pressure gradients. Reference — ; Laminar - - - - ; case1 — ; case2 — ; case3 — ; case4 — ; case5 — ; case6 — ; case7 — ; case8 — ; case9 — ; case10 — ; case11 —

Observing Fig.2, two different behaviours can be identified: re-laminarization and turbulent cases. *case01*, *case02*, *case03* and *case11* become laminar, converging to a given mean streamwise pressure gradient and remaining in this regime until the end of the simulations. The rest of peristalsis cases remain turbulent, showing a noisy solution for the whole extent of the simulations. Note that the mean pressure gradients presented account for both the external pressure gradient responsible for pumping the flow and the peristaltic contribution. Nakanishi et. al. (2012) present the time traces of the external pressure gradient only, and even if the best performing cases coincide with the ones

computed with the in-house DNS code, a quantitative comparison cannot be established. The validation of the obtained solution based on dissipation is presented in the Sec.3.5.

3.3. Laminar cases

In this section, *case1*, *case2* and *case3* are presented in detail to assess the cases that become laminar when peristalsis is applied. *tke* is defined as half the trace of Reynolds stress tensor:

$$tke = \frac{1}{2} \left(\overline{(u')^2} + \overline{(v')^2} + \overline{(w')^2} \right) \quad (4)$$

Where $\overline{(u')^2}$, $\overline{(v')^2}$ and $\overline{(w')^2}$ are the variances of the streamwise, spanwise and wall-normal velocity fluctuations respectively. Fig.3 shows the time history of *tke* for cases 1,2,3 together with the reference turbulent channel flow.

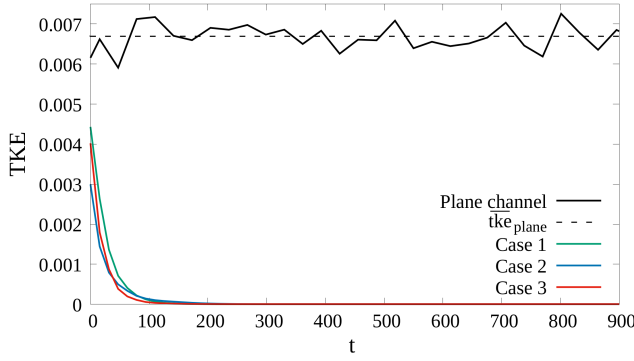


Figure 3: Time history of *tke* for re-laminarization cases

It can be clearly seen how the controlled cases tend to a laminar regime after approximately 200 external time units, and remain laminar until the end of the simulation. This behaviour can also be visualized in Fig.4, which presents the mean velocity profiles at different streamwise positions and time instants (initial and final) for *case01*, the turbulent plane channel and the laminar plane channel. At $t = 0 \frac{h}{U_b}$ the instantaneous mean velocity profile of *case01* presents a flattened shape characteristic of turbulent mean velocity profiles, and resembles the shape of the mean profiles for the reference plane channel case. Once re-laminarization is achieved the velocity profile shows a parabolic-like shape that tends to the Poiseuille laminar profiles. Reverse flow can be observed for the controlled velocity profile at streamwise location $x = 2.5$, which

according to [1] it is a consequence of the boundary movement that is responsible for transferring fluid particles in closed loop tracks.

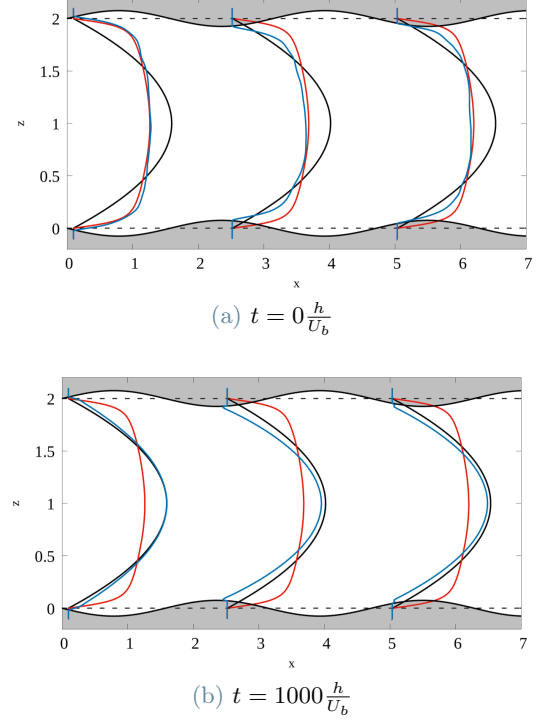


Figure 4: Velocity field of *case01* in the x-z plane

3.4. Turbulent cases

For the sake of simplicity, the time history of *tke* is presented for *case04* and *case05*, while mean velocity profiles and *r.m.s* of turbulent intensities are presented only for *case04*. The rest of turbulent cases are accounted for at the net-power saving study in Sec.3.5. Both *case04* and *case05* remain turbulent until the end of the simulation as seen in Fig.5, but they present a lower *tke* with respect to the reference case for the complete time history.

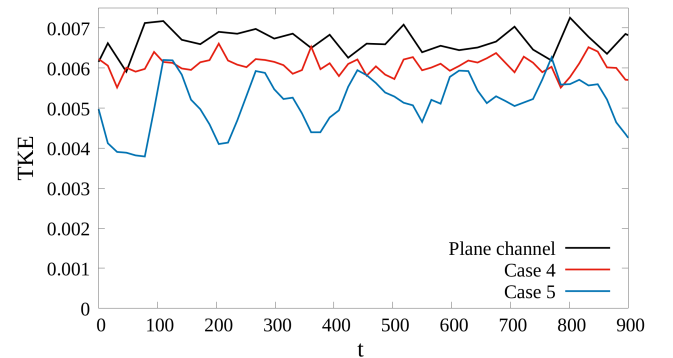


Figure 5: Time history of *tke* for turbulent cases

This reduction indicates that even if they remain turbulent, ordinary turbulent drag reduction is achieved. For this cases, the mean velocity profiles remained with the characteristic flattened shape of turbulent profiles for the whole extent of the simulation.

In Fig.6, *r.m.s* instantaneous fluctuating velocity component normalized with bulk velocity of *case04* are presented for three streamwise locations (points of minimum, null and maximum height of the peristalsis waves). The reference case *r.m.s* components are also presented for comparison. It can be confirmed that the introduction of non-planar moving walls have an impact on the wall vicinity in terms of velocity fluctuations. For the streamwise positions corresponding to the lowest and highest points in the wall ($x=1.5$ and $x=4.5$ respectively), the profiles are shifted towards z -negative values for $x=1.5$ and towards z -positive values for $x=4.5$. In the streamwise location $x=2$ (no effective wall amplitude), the profiles resemble those corresponding to the plane channel, with only a small increase for the streamwise component's peak, and a slight reduction for the other two components. The largest reduction of turbulent intensity is visible for the streamwise location $x=4.5$, with lower intensity peaks with respect to the plane channel. Reynolds shear stress $-\overline{u'w'}$ plays a crucial role in drag reduction applications. Its decrease could lead to a re-laminarized flow and, eventually, sub-laminar drag as deduced from Eq.5:

$$C_f = \frac{12}{Re_b} + 24 \int_0^1 (1-z)(-\overline{u'w'})dz \quad (5)$$

Given its importance in non-planar moving walls applications, Reynolds shear stresses for *04* for the same streamwise locations studied for the *r.m.s* analysis are presented in 7. The highly irregular shapes of the profiles is because the data presented (except for the reference case) is instantaneous. It's clear that $-\overline{u'w'}$ is reduced with respect to the reference case, demonstrating again that peristalsis is capable to modify the behaviour of the flow at the wall-vicinity. Negative RSS can be observed for both cases at location $x=3$ and at $x=1.5$. This phenomenon is crucial for drag reduction because the more negative RSS are, the higher the reduction of skin-friction.

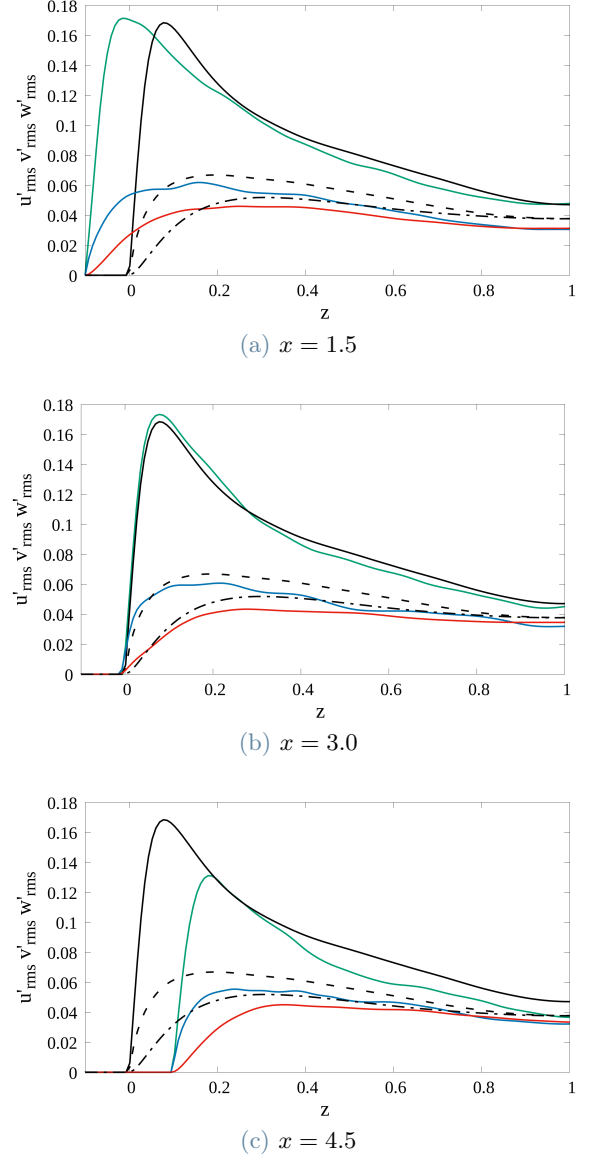


Figure 6: Instantaneous root mean square fluctuation velocity components for *case04* at three different streamwise locations

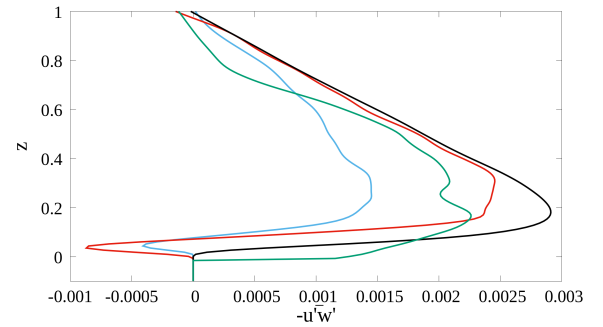


Figure 7: Reynolds shear stresses for *case04* (left) and *case05* (right). $x=1.5$ — blue ; $x=3$ — red ; $x=4.5$ — green

3.5. Net power savings

The assessment of the net power savings has been performed using the total dissipation ε , which can be described as:

$$\varepsilon = \frac{2}{Re_b V} \int_V \mathbf{S} : \mathbf{S} dV \quad (6)$$

The net power saving rate is computed with Eq.7 accounting for the time averaged total dissipation for the reference plane channel case ε_{ref} and for the controlled cases with $\bar{\varepsilon}$.

$$S = \frac{\bar{\varepsilon}_{ref} - \bar{\varepsilon}}{\bar{\varepsilon}_{ref}} \times 100[\%] \quad (7)$$

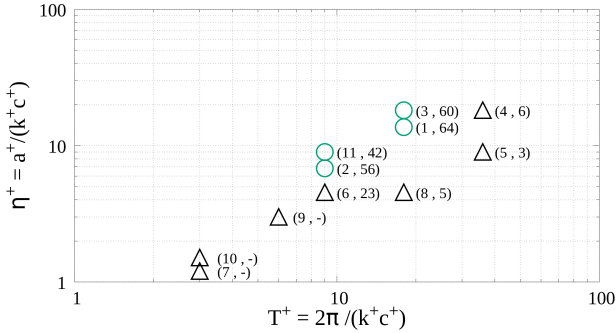


Figure 8: Net power saving rate map as function of peristalsis inputs

The computed values for the net power saving rates are presented in Fig.8, where the horizontal axis is the deformation period in wall units and the vertical axis is the displacement amplitude in both units. The numbers in the left of the parenthesis are the case identification number and the values on the right are the net power saving rates computed, while green circles refer to re-laminarized cases and black triangles to turbulent cases. The re-laminarization and ordinary drag reduction cases with larger net power saving rate are *case01* with $S = 64\%$ and *case06* with $S = 23\%$, respectively. It's important to highlight how the best performing cases are localized in a certain region of the map. This region corresponds to $T^+ > 8$ and $T^+ < 20$ with respect to the horizontal axis, and $\eta^+ > 5$ and $\eta^+ < 20$ for the vertical axis. These results suggest that relaminarization occurs under relatively large amplitudes of velocity a and wavenumber k . However, if the mentioned quantities are further increased, the flow cannot

be relaminarized. It can also be observed how very large wave propagation speeds result in no net power savings, as it occurs for *case07* and *case10*.

Tab.3 collects the net power savings computed and its targeted value presented in [3]. It can be stated that the computed values are in accordance with the expected solution, and that the in-house DNS code is able to properly capture the dynamics in the wall-vicinity with the IB method. The computation of the net power savings S was done exploiting the dissipation definition both for the reference and in the present Thesis. Dissipation at the statistically steady state is defined as the sum of friction power, pressure power and input power. Therefore, the slight difference in the results in Tab.3 doesn't arise from the inclusion of the peristalsis contribution in the mean pressure gradient, but from differences in the numerical approaches implemented.

	S in %	S in [3] in %
Case 1	64	65
Case 2	56	53
Case 3	60	59
Case 4	6	4
Case 5	3	-
Case 6	23	21
Case 7	-	-
Case 8	5	5
Case 9	-	-
Case 10	-	-
Case 11	42	not presented

Table 3: Comparison between net power savings in % for the in-house DNS code and data reported in [3]

4. Conclusions

Fully developed turbulent channel flows controlled by means of streamwise traveling waves of wall deformation have been studied with the aim to validate an in-house DNS code as well as to further understand how the flow behaves in the presence of peristalsis waves, and its contribution to net power savings. The in-house DNS solver exploits the Immersed Boundary method over a fixed Cartesian grid for the solid boundaries treatment, leading to a more efficient performance as well as lower memory usage. Previously to the validation of the code, the paralleli-

sation scheme has been updated with the MPI library introduction, and a scaling performance analysis has been conducted to use efficiently the HPC resources dedicated to this project.

The solutions obtained are in agreement with the data reported in [3], with the same cases achieving relaminarization except for *case11*, where the cyclical transition from laminar to turbulent and vice versa could not be captured. *case01*, *case02*, *case03* and *case11* become laminar after a relatively short time, while some cases like *case06* and *case04* present net power savings even if they are turbulent for the whole extent of the simulations. The largest net power saving among all cases studied is achieved for *case01*, with a net power saving of the 64%, while the largest power saving for ordinary drag reduction cases corresponds to *case06*, with 23%. In addition, all the re-laminarization cases have been localized for the input parameters defining the region $\eta^+ > 5$ and $\eta^+ < 20$ and $T^+ > 8$ and $T^+ < 20$ in the Net power saving rates map. It has been proven that the implementation followed is able to have a direct impact in the wall vicinity region, as showed by the *rms* fluctuation velocity and Reynolds shear stress, and that the controlled influence on this region can lead to substantial net power savings for turbulent channel flows.

References

- [1] J Hoepffner and K Fukagata. Pumping or drag reduction? *Journal of Fluid Mechanics*, (635):171–187, 2009.
- [2] J Kim, P Moin, and R Moser. Turbulence statistics in fully developed channel flow at low reynolds number. *Journal of Fluid Mechanics*, (177):133–166, 1987.
- [3] R Nakanishi, H Mamori, and K Fukagata. Relaminarization of turbulent channel flow using traveling wave-like wall deformation. *International Journal of Heat and Fluid Flow*, (35):152–159, 2012.
- [4] Francesco Secchi. Immersed boundary simulation of turbulent flow through a peristaltic actuator. Master’s thesis, Politecnico di Milano, 2018.